


 Cite this: *RSC Adv.*, 2023, **13**, 13142

# *In situ* formation of red/black phosphorus-modified SiO<sub>2</sub>@g-C<sub>3</sub>N<sub>4</sub> multi-heterojunction for the enhanced photocatalytic degradation of organic contaminants†

 Jiancheng Li,<sup>abc</sup> Chi Wang,<sup>ID \*abc</sup> Yixing Ma,<sup>\*d</sup> Kai Li<sup>ID d</sup> and Yi Mei<sup>abc</sup>

A new heterojunction material BP/RP-g-C<sub>3</sub>N<sub>4</sub>/SiO<sub>2</sub> was obtained by a one-step ball milling method, and its photocatalytic capacity was researched by the degradation of Rhodamine B (RhB) and ofloxacin (OFL) in simulated sunlight. The construction of an *in situ* BP/RP heterojunction can achieve perfect interface contact between different semiconductors and effectively promote the separation of photogenerated carriers. The composite material was well characterized, which proved that the multi-heterogeneous structure was prepared. Furthermore, the type II heterojunction was formed between the g-C<sub>3</sub>N<sub>4</sub> and BP/RP interface, playing an important role in the degradation and promoting electron transfer. The degradation effect of BP/RP-g-C<sub>3</sub>N<sub>4</sub>/SiO<sub>2</sub> on RhB reached 90% after 26 min of simulated solar irradiation, which was 1.8 times that of g-C<sub>3</sub>N<sub>4</sub>/SiO<sub>2</sub>. The degradation of OFL by BP/RP-g-C<sub>3</sub>N<sub>4</sub>/SiO<sub>2</sub> reached 85.3% after illumination for 50 min, while the degradation of g-C<sub>3</sub>N<sub>4</sub>/SiO<sub>2</sub> was only 35.4%. The mechanisms were further discussed, and <sup>•</sup>O<sub>2</sub><sup>-</sup> and h<sup>+</sup> were found to be the main active substances to degrade RhB. The catalyst also revealed distinguished stability of catalyst and recyclability, and the degradation effect of RhB can still realize 85% after 4 runs of experiment. Thus, this study provided a novel method for the design and preparation of multi-heterojunction catalysts in the removal of organic pollutants from wastewater.

 Received 21st March 2023  
 Accepted 14th April 2023

DOI: 10.1039/d3ra01850d

[rsc.li/rsc-advances](https://rsc.li/rsc-advances)

## 1. Introduction

Dyes discharged with industrial wastewater as the main organic pollutants cause harm to the environment. Carcinogenic dyes endanger human health.<sup>1</sup> Antibiotics are widely used to treat bacterial infections in humans and animals.<sup>2–4</sup> Ofloxacin (OFL), one of the fluoroquinolones, in medical wastewater is not biodegradable.<sup>5</sup> As a result, OFL will accumulate in surface water.<sup>6</sup> Therefore, the development of treatment methods for the removal of dyes and antibiotics from wastewater is urgently required.

Various traditional methods have been used to degrade organic pollutants. However, there will be problems such as

poor degradation effect or high costs. Adsorption and coagulation techniques remove dye and antibiotics by converting them to solid substances from a liquid state, which will cause secondary damage to the environment.<sup>7</sup> Alternatively, advanced oxidation processes (AOPs), such as electrochemical oxidation, ultraviolet (H<sub>2</sub>O<sub>2</sub>), gamma ray/electron beam radiation, photochemical oxidation, ozonation (O<sub>3</sub>/H<sub>2</sub>O<sub>2</sub>), Fenton/photo-Fenton, persulfate-based oxidation, and ultrasonic oxidation, have been widely used as advanced treatment processes for the degradation of organic pollutants in wastewater.<sup>8–11</sup> The removal of both antibiotics<sup>12–14</sup> and organic dyes<sup>15–19</sup> by various AOPs has been reported. Interestingly, semiconductor photocatalysis has been considered as one of the most promising clean technologies for the removal of organic pollutants in a short period of time.<sup>20</sup> Photocatalytic technology has the characteristics of mild reaction conditions and green environmental protection and has attracted much attention in dye wastewater treatment technology.<sup>21</sup>

As an inorganic non-metallic material, graphitic carbon nitride (g-C<sub>3</sub>N<sub>4</sub>, CN) has been widely used in the degradation of organic pollutants due to its superior physical and chemical properties.<sup>22–24</sup> However, the photocatalytic efficiency of g-C<sub>3</sub>N<sub>4</sub> is low due to its low utilization of visible light and high recombination rate of photogenerated electron-hole pairs in

<sup>a</sup>Faculty of Chemical Engineering, Kunming University of Science and Technology, Kunming City 650500, China. E-mail: wangchikg@163.com; Tel: +86-159 2512 8686

<sup>b</sup>Yunnan Province Key Laboratory of Energy Saving in Phosphorus Chemical Engineering and New Phosphorus Materials, Kunming City 650500, China

<sup>c</sup>The Higher Educational Key Laboratory for Phosphorus Chemical Engineering of Yunnan Province, Kunming City 650500, China

<sup>d</sup>Faculty of Environmental Science Engineering, Kunming University of Science and Technology, Kunming City 650500, China. E-mail: 835322020@qq.com; Tel: +86-187 8810 3059

† Electronic supplementary information (ESI) available. See DOI: <https://doi.org/10.1039/d3ra01850d>



photocatalytic reactions.<sup>25–27</sup> At present, g-C<sub>3</sub>N<sub>4</sub> is modified by metal deposition,<sup>28</sup> element doping,<sup>29</sup> and heterojunction construction.<sup>30</sup> Among them, the construction of a heterojunction based on g-C<sub>3</sub>N<sub>4</sub> is a feasible method to solve the problem of rapid recombination of g-C<sub>3</sub>N<sub>4</sub> photogenerated carriers.<sup>31–33</sup>

As the most abundant substance on the earth, SiO<sub>2</sub> not only promotes the adsorption of organic matter, but also promotes the migration of photogenerated carriers on the surface of g-C<sub>3</sub>N<sub>4</sub> when forming a heterostructure with g-C<sub>3</sub>N<sub>4</sub>.<sup>34–36</sup> On the basis of the previous research of the research group, the addition of SiO<sub>2</sub> also helps to increase the yield of g-C<sub>3</sub>N<sub>4</sub>. Although SiO<sub>2</sub> has this effect in the formation of a heterojunction, it does not fully release the potential in the photocatalytic degradation of g-C<sub>3</sub>N<sub>4</sub>.<sup>37</sup> Therefore, we need to introduce additional materials to overcome the current difficulties and integrate the advantages of all components in the hope of achieving better performance.

The catalytic activity of g-C<sub>3</sub>N<sub>4</sub> is enhanced when added to RP. The visible light utilization capacity of RP/g-C<sub>3</sub>N<sub>4</sub> is 1.33 times greater than that of the original g-C<sub>3</sub>N<sub>4</sub>, indicating that the heterojunction can effectively utilize the enhanced light, highlighting the importance of the type I heterojunction formed between RP and g-C<sub>3</sub>N<sub>4</sub> (accelerating the separation of photogenerated carriers and broadening the absorption range of visible light).<sup>38</sup> It was reported recently that black phosphorus (BP), as an emerging nonmetallic two-dimensional (2D) material, has an adjustable band gap, fast photogenerated carrier mobility ( $\sim 1000 \text{ cm}^2 \text{ V}^{-1} \text{ s}^{-1}$ ) and high conductivity (approximately  $10^2 \text{ S m}^{-1}$ ).<sup>39–42</sup> In the field of optoelectronics, BP nanosheets prepared by mechanical method have been applied.<sup>43</sup> This is due to the fact that BP-based heterostructures can efficiently separate photogenerated carriers, while maintaining the stability of BP.<sup>44</sup> For example, Zhu *et al.* used the excellent electron transfer ability of BP/CN in the photolysis of water for hydrogen evolution.<sup>45</sup> Eroglu *et al.* used the synergistic effect of the FLBP/g-CN heterojunction interface to photo-oxidize organic compounds.<sup>46</sup> He *et al.* used BP-CN to efficiently kill bacteria in water.<sup>47</sup> In all heterojunctions, heterostructures formed by a single element can produce strong interfacial forces and close contacts.<sup>48</sup> Using ball milling technology to convert RP into BP/RP heterostructure can prolong the service life of electron-hole pairs and improve the degradation efficiency of pollutants. It is possible to combine BP/RP with g-C<sub>3</sub>N<sub>4</sub>/SiO<sub>2</sub> to form an efficient heterostructure.

In our work, a novel multi-material heterostructure BP/RP-g-C<sub>3</sub>N<sub>4</sub>/SiO<sub>2</sub> was prepared by ball milling. RhB and OFL were selected as typical organic compounds to study the photoelectric properties of BP/RP-g-C<sub>3</sub>N<sub>4</sub>/SiO<sub>2</sub> and electron transfer in multi-heterogeneous structures. Due to the formation of the P-C bond between g-C<sub>3</sub>N<sub>4</sub>/SiO<sub>2</sub> and BP/RP, the composites showed good photocatalytic performance. The P-C bonds extend the life of the photogenerated electrons in the whole system. Finally, the mechanism of photocatalysis is estimated and the active substances are tested.

## 2. Experimental sections

### 2.1. Chemical reagents

The principal chemicals include urea (Tianjin Fengchuan Chemical Reagent Technology Co. Ltd), ethanol, silica dioxide (Aladdin), RP (Sinopharm Chemical Reagent Co. Ltd), RhB (C<sub>28</sub>H<sub>31</sub>ClN<sub>2</sub>O<sub>3</sub>, Sinopharm Chemical Reagent Co. Ltd), OFL (C<sub>18</sub>H<sub>20</sub>FN<sub>3</sub>O<sub>4</sub>, Maya Reagent), acetonitrile (C<sub>2</sub>H<sub>3</sub>N, Maya Reagent) and others.

### 2.2. Synthesis of composite

The synthesis of BP/RP-g-C<sub>3</sub>N<sub>4</sub>/SiO<sub>2</sub> catalytic materials is shown in Fig. 1. In a typical synthesis, deionized water was added to the ceramic crucible, 3.0 g urea and a certain amount of SiO<sub>2</sub> were added, and ultrasonic stirring was performed at room temperature for 0.5 h. The ceramic crucible was placed on a magnetic stirrer and heated at a speed of 150 rpm for 0.5 h to obtain a solid material. A total of 5.0 g urea was placed into a ceramic crucible and heated at 550 °C for 2 h with a heating speed of 5 °C min<sup>-1</sup> in a muffle furnace, then cooled naturally to room temperature. The g-C<sub>3</sub>N<sub>4</sub> containing 200 mg of SiO<sub>2</sub> is denoted as g-C<sub>3</sub>N<sub>4</sub>/SiO<sub>2</sub>.

A total of 3 g of red phosphorus was placed in a Teflon-lined reaction kettle with 60 ml of deionized water (200 °C with a heating rate of 5 °C for 12 h, and cooled down to room temperature naturally). After filtration, the samples were dried in a vacuum oven at 30 °C. The solid powder with oxide layer removed was then obtained.

BP/RP-g-C<sub>3</sub>N<sub>4</sub>/SiO<sub>2</sub> was prepared by ball-milling. The oxide-free RP and g-C<sub>3</sub>N<sub>4</sub>/SiO<sub>2</sub> were placed in a tank with agate balls of different diameters, and ball-milled at a speed of 450 rpm. A certain amount of RP to remove oxidation layer was added to g-C<sub>3</sub>N<sub>4</sub>/SiO<sub>2</sub> for ball milling. A total of 10% of RP was added and denoted as 10RP-g-C<sub>3</sub>N<sub>4</sub>/SiO<sub>2</sub>. The ratio of agate ball to sample was 30 : 1. A total of 40% RP material was added to g-C<sub>3</sub>N<sub>4</sub>/SiO<sub>2</sub> and ball-milled for 12 h at 450 rpm, and called BP/RP-g-C<sub>3</sub>N<sub>4</sub>/SiO<sub>2</sub>.

### 2.3. Characterization

The synthesized catalysts were analyzed and characterized by X-ray diffraction (XRD, X'Pert-3, Panalytical, Netherlands), transmission electron microscopy (TEM, Tecnaï G2 F20, FEI, USA), Raman spectroscopy, X-ray photoelectron spectroscopy (XPS, K-Alpha, Thermo Fisher Scientific, USA), Fourier transform infrared (FT-IR, Tensor, Bruke) spectroscopy, thermogravimetric analysis (TGA, STA449, Netzsch), UV-vis diffuse reflectance spectroscopy (UV-vis, TU-1901, Persee, China), photoluminescence spectra (PL, FLS1000, Edinbrugh), Raman spectroscopy (Renishaw, UK) and other methods.

### 2.4. Photoelectrochemistry experiments

Electrochemical impedance spectroscopy (EIS), photocurrent test (*I*-*t*) and a conventional three-electrode electrochemical workstation were used to test the Mott-Schottky plots. Details are provided in the ESI.†



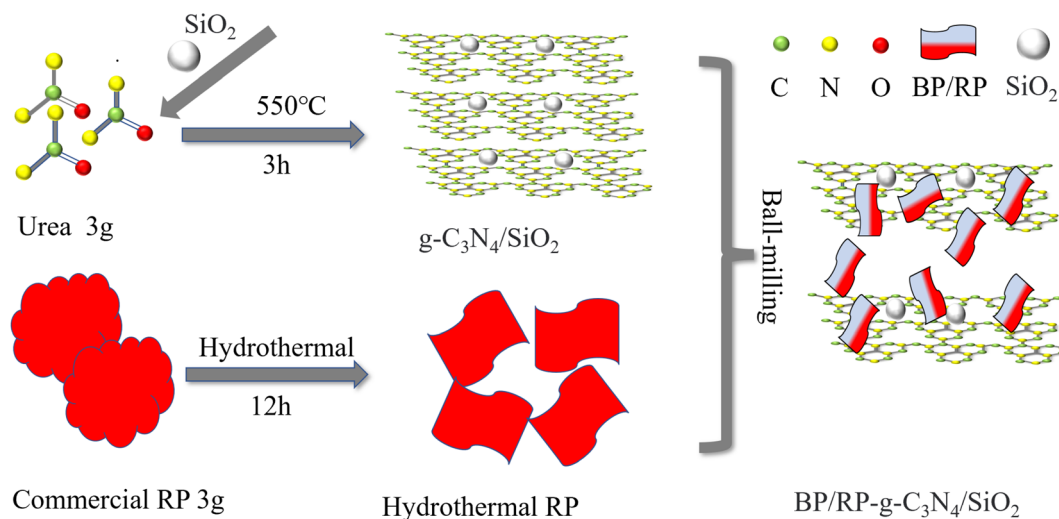


Fig. 1 Schematic diagram of the BP/RP-g-C<sub>3</sub>N<sub>4</sub>/SiO<sub>2</sub> composites.

### 2.5. Photocatalytic degradation experiment

The prepared catalyst was tested. Before photodegradation, dark adsorption equilibrium experiments were first performed on organic matter. It was found that the adsorption equilibrium of RhB was reached in 10 min, and the proportion of adsorption equilibrium was not more than 5%. The results showed that the adsorption equilibrium of OFL was reached within 30 min, and the adsorption equilibrium ratio was not more than 20%. Then, the photocatalytic experiment was carried out under a 350 W

xenon lamp, and a sample was taken every 4 min, and centrifugation was carried out. The experimental operation was carried out with an ultraviolet spectrophotometer. The calculation of photocatalysis is determined by the following eqn (1) and (2):

$$y = C/C_0 \quad (1)$$

$$-\ln(C/C_0) = kt \quad (2)$$

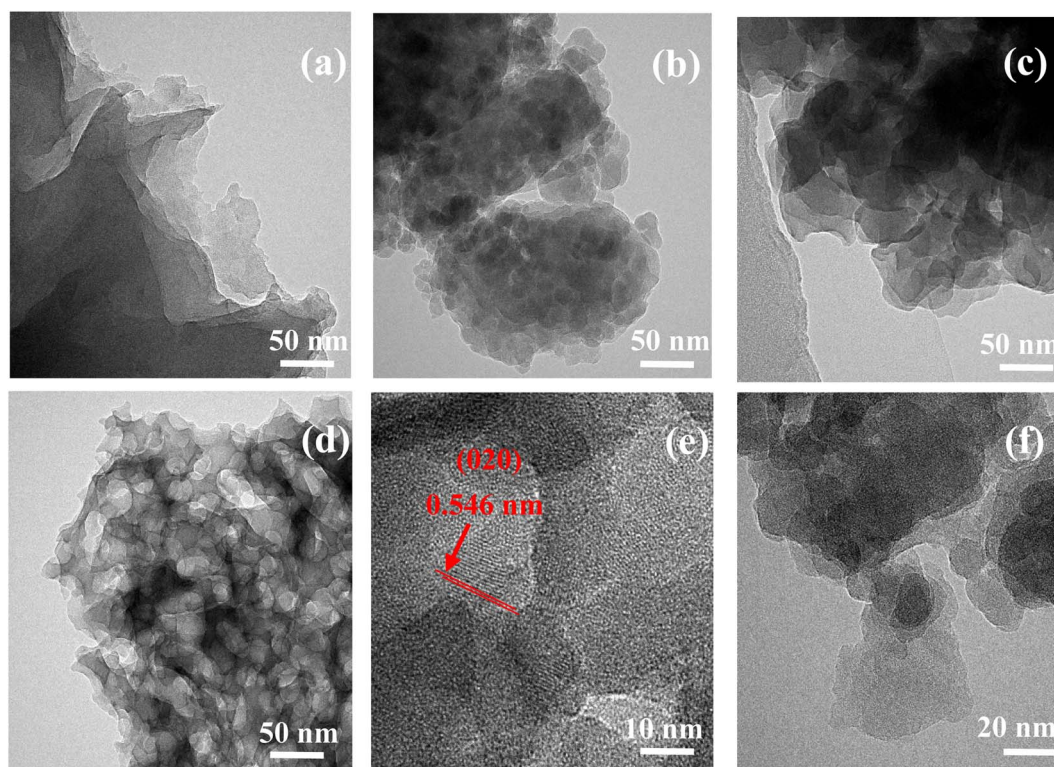


Fig. 2 TEM of (a) g-C<sub>3</sub>N<sub>4</sub>, (b) g-C<sub>3</sub>N<sub>4</sub>/SiO<sub>2</sub>, (c) RP, (d) and (e) BP/RP, (f) BP/RP-g-C<sub>3</sub>N<sub>4</sub>/SiO<sub>2</sub>.



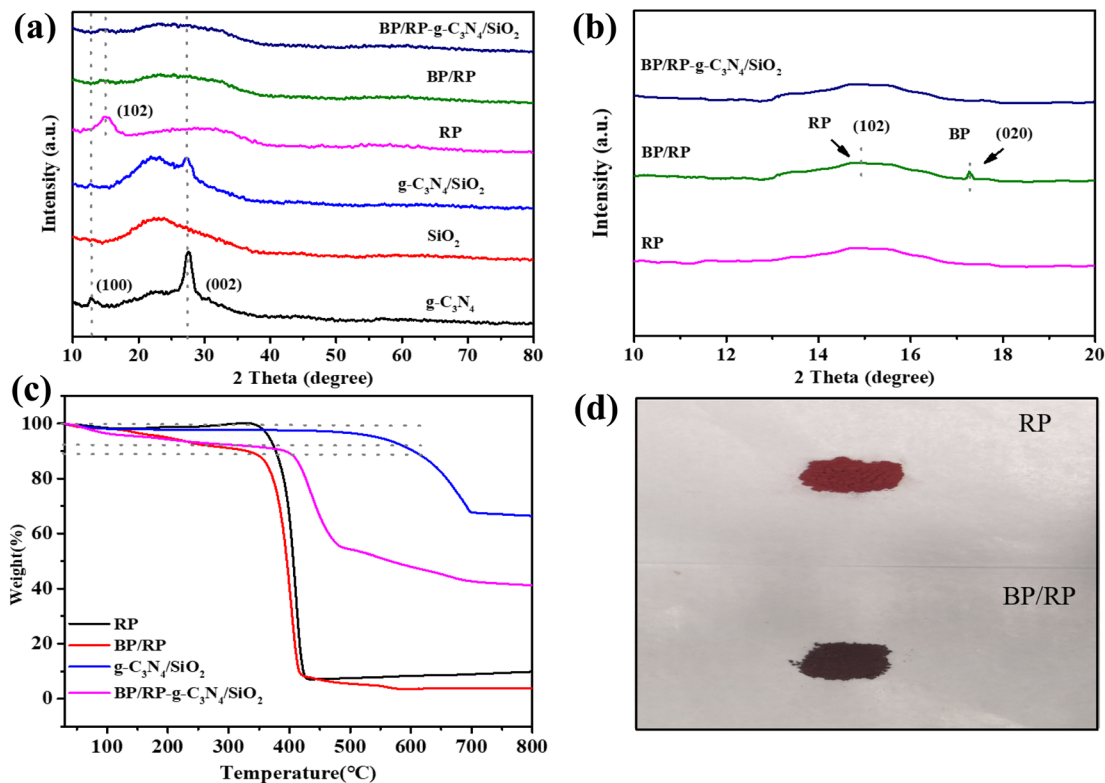


Fig. 3 XRD patterns of (a)  $g\text{-C}_3\text{N}_4$ ,  $\text{SiO}_2$ ,  $g\text{-C}_3\text{N}_4/\text{SiO}_2$ , RP, BP/RP, BP/RP- $g\text{-C}_3\text{N}_4/\text{SiO}_2$  samples, (b) enlarged XRD of RP, BP/RP and BP/RP- $g\text{-C}_3\text{N}_4/\text{SiO}_2$  samples, (c) TGA curves of  $g\text{-C}_3\text{N}_4/\text{SiO}_2$ , RP, BP/RP, BP/RP- $g\text{-C}_3\text{N}_4/\text{SiO}_2$  samples, (d) comparison before and after ball milling RP.

where  $C$  is the solubility of the solution after the light time  $t$ ,  $C_0$  is the concentration before dark reaction adsorption, and  $k$  is the rate constant ( $\text{min}^{-1}$ ).

In each of the degradation experiments, the prepared 2 mg solid catalyst was added to 40 ml of solution containing RhB ( $60 \text{ mg L}^{-1}$ ). OFL was degraded, the amount of catalyst was 5 mg/40 ml, the amount of OFL was  $10 \text{ mg L}^{-1}$ , and the samples were tested by liquid chromatography. The mobile phase was

acetonitrile and 0.8% glacial acetic acid (75:25). The test wavelength was 289 nm.

### 3. Results and discussion

#### 3.1. Construction of BP/RP- $g\text{-C}_3\text{N}_4/\text{SiO}_2$

The TEM image shows the morphology of the material in Fig. 2. As displayed in Fig. 2a,  $g\text{-C}_3\text{N}_4$  has a layered fold morphology. In

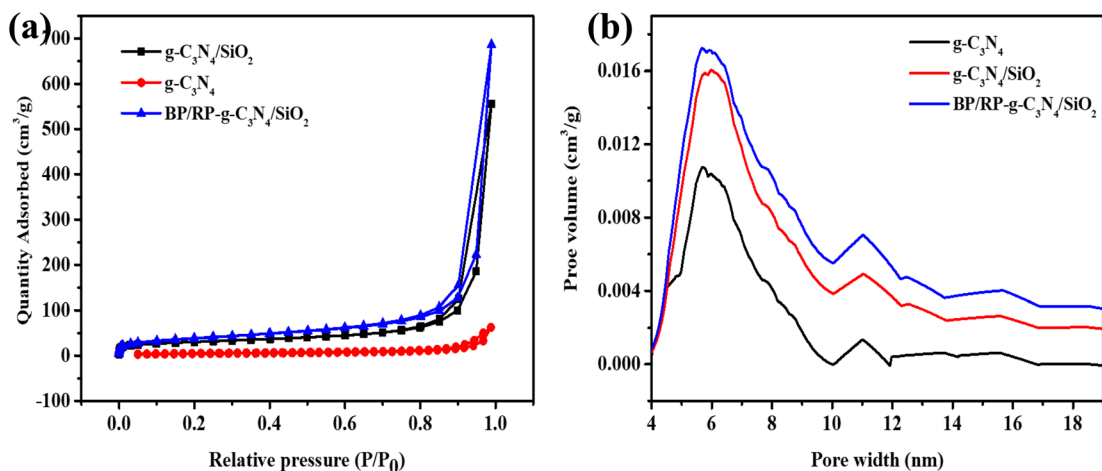


Fig. 4 (a)  $\text{N}_2$  adsorption-desorption curve of  $g\text{-C}_3\text{N}_4$ ,  $g\text{-C}_3\text{N}_4/\text{SiO}_2$  and BP/RP- $g\text{-C}_3\text{N}_4/\text{SiO}_2$ . (b) Pore size distribution of  $g\text{-C}_3\text{N}_4$ ,  $g\text{-C}_3\text{N}_4/\text{SiO}_2$  and BP/RP- $g\text{-C}_3\text{N}_4/\text{SiO}_2$ .



Fig. 2b, the addition of spherical SiO<sub>2</sub> leads to the presence of speckles on the surface of g-C<sub>3</sub>N<sub>4</sub>. In the same amorphous lamellar RP (Fig. 2c), stripping occurred after ball milling and a (020) BP lattice fringe was formed (Fig. 2d and e), indicating that the BP/RP heterostructure was successfully prepared. A multi-component composite containing BP/RP can be observed in Fig. 2f. All of the materials have a layered structure, which is also consistent with the previous literature. SEM shows that the BP/RP-g-C<sub>3</sub>N<sub>4</sub>/SiO<sub>2</sub> lamella decreased, and all kinds of substances were evenly distributed (Fig. S1 and S2†).

The crystal structures of the as-prepared g-C<sub>3</sub>N<sub>4</sub>, SiO<sub>2</sub>, g-C<sub>3</sub>N<sub>4</sub>/SiO<sub>2</sub>, RP, BP/RP, and BP/RP-g-C<sub>3</sub>N<sub>4</sub>/SiO<sub>2</sub> were investigated using XRD. For pure g-C<sub>3</sub>N<sub>4</sub>, the distinct characteristic diffraction peaks at 13.7° and 27.6° were indexed to the typical triazine interring accumulation peak (100) and interlayer accumulation peak (002), respectively.<sup>49</sup> The structures of g-C<sub>3</sub>N<sub>4</sub> are usually stacked in layers.<sup>50,51</sup> After adding SiO<sub>2</sub>, a new characteristic peak of g-C<sub>3</sub>N<sub>4</sub>/SiO<sub>2</sub> appeared at 23°, which is consistent with the characteristic peak position shown in the XRD pattern of pure SiO<sub>2</sub>. In addition, no other characteristic peaks were found, indicating that the structure of g-C<sub>3</sub>N<sub>4</sub> did not change with the addition of SiO<sub>2</sub>. Fig. 3a shows the XRD patterns of RP. It is known that RP forms peaks at 15.2°, 30.0° and 57.5° (JCPDS 44-0906). The characteristic peak of 17.2° in the XRD of BP is the

(020) plane, 28.8° is the (021) plane and 33.9° is the (040) plane.<sup>52</sup> In BP/RP, there is a 17.2° peak in addition to 15.2° (Fig. 3b). According to the TEM characterization (Fig. 2e), 17.2° in BP/RP represents the (020) plane of BP (JCPDS 73-1358). In BP/RP-g-C<sub>3</sub>N<sub>4</sub>/SiO<sub>2</sub>, the characteristic peak of BP was not obvious. The reason for this phenomenon may be that less BP is produced during the formation of the heterojunction. The color change of the sample after ball milling is also a good indication (Fig. 3d).

TGA was used to roughly estimate the weight percent of BP in the heterostructure (Fig. 3c). SiO<sub>2</sub> has a high melting point, and g-C<sub>3</sub>N<sub>4</sub> can be thermally exfoliated at a certain temperature, releasing gas and causing mass loss of g-C<sub>3</sub>N<sub>4</sub>.<sup>53</sup> The mass of RP began to decrease until 350 °C. At 150 °C, the masses of the BP/RP and BP/RP-g-C<sub>3</sub>N<sub>4</sub>/SiO<sub>2</sub> composites began to decrease. The decrease in the low temperature region may be due to the presence of BP in the composites. The mass fraction of BP in BP/RP and BP/RP-g-C<sub>3</sub>N<sub>4</sub>/SiO<sub>2</sub> can then be calculated by the following formula:<sup>54</sup>

$$\text{BP (\%)} = \frac{M_s - M_{\text{RP}}}{M} \times 100\% \quad (3)$$

where BP (%) represents the mass fraction of BP in the composite,  $M_s$  represents the residual mass of the composite

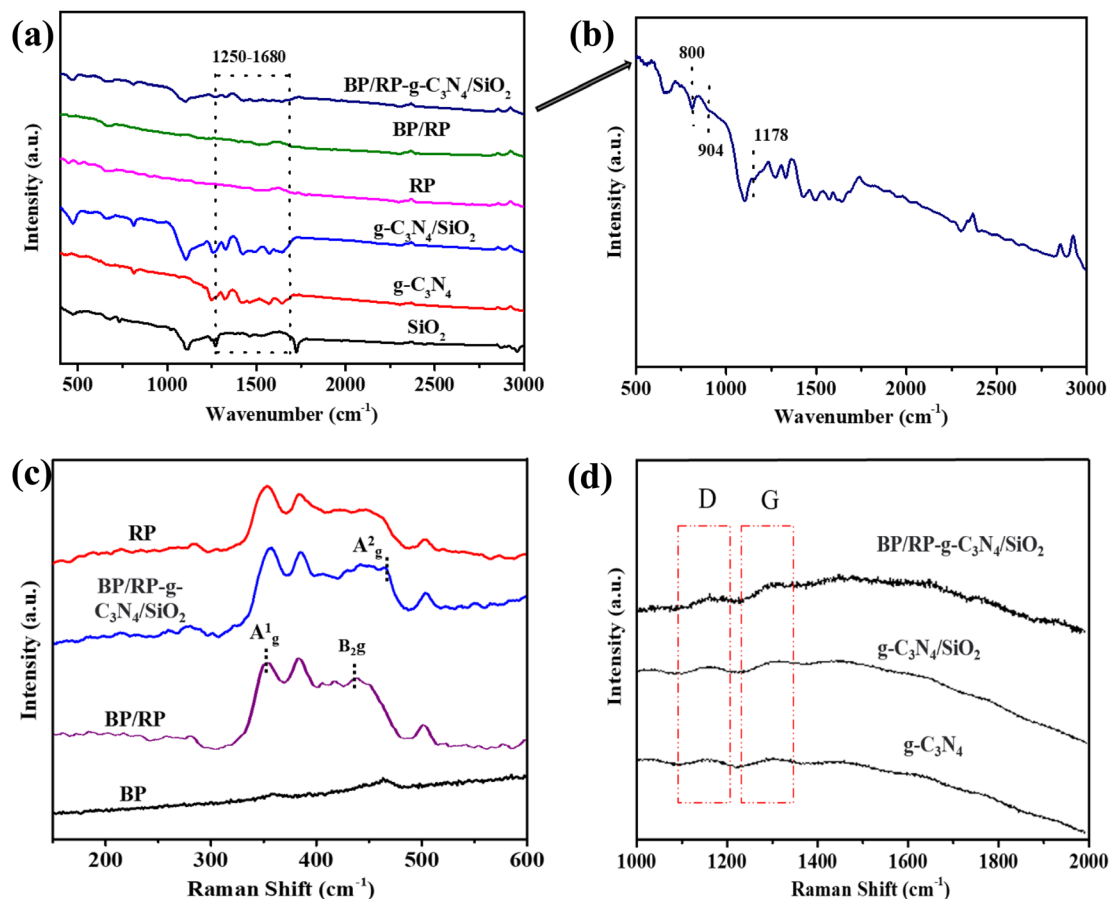


Fig. 5 (a) FT-IR spectra of g-C<sub>3</sub>N<sub>4</sub>, g-C<sub>3</sub>N<sub>4</sub>/SiO<sub>2</sub>, RP, BP/RP and BP/RP-g-C<sub>3</sub>N<sub>4</sub>/SiO<sub>2</sub>. (b) FT-IR enlarged spectra of BP/RP-g-C<sub>3</sub>N<sub>4</sub>/SiO<sub>2</sub>. (c) Raman shift of RP, BP, BP/RP and BP/RP-g-C<sub>3</sub>N<sub>4</sub>/SiO<sub>2</sub>. (d) Raman shift of g-C<sub>3</sub>N<sub>4</sub>, g-C<sub>3</sub>N<sub>4</sub>/SiO<sub>2</sub> and BP/RP-g-C<sub>3</sub>N<sub>4</sub>/SiO<sub>2</sub>.



when the heat loss begins,  $M_{RP}$  represents the residual mass of the composite when the heat loss begins, and  $M$  represents the total mass. Therefore, BP may contain 8% in BP/RP and 4% in BP/RP-g-C<sub>3</sub>N<sub>4</sub>/SiO<sub>2</sub>.

The N<sub>2</sub> adsorption-desorption isotherms of g-C<sub>3</sub>N<sub>4</sub>, g-C<sub>3</sub>N<sub>4</sub>/SiO<sub>2</sub> and BP/RP-g-C<sub>3</sub>N<sub>4</sub>/SiO<sub>2</sub> were measured. As shown in Fig. 4a, the N<sub>2</sub> adsorption isotherms of g-C<sub>3</sub>N<sub>4</sub>, g-C<sub>3</sub>N<sub>4</sub>/SiO<sub>2</sub> and BP/RP-g-C<sub>3</sub>N<sub>4</sub>/SiO<sub>2</sub> have a typical H3-type hysteresis loop, which belongs to the type IV isotherm.<sup>55-57</sup> The pore sizes of g-C<sub>3</sub>N<sub>4</sub>, g-C<sub>3</sub>N<sub>4</sub>/SiO<sub>2</sub> and BP/RP-g-C<sub>3</sub>N<sub>4</sub>/SiO<sub>2</sub> are mostly distributed in the range of 4–10 nm (Fig. 4b), indicating that mesoporous structures exist in g-C<sub>3</sub>N<sub>4</sub>, g-C<sub>3</sub>N<sub>4</sub>/SiO<sub>2</sub> and BP/RP-g-C<sub>3</sub>N<sub>4</sub>/SiO<sub>2</sub>. Compared with g-C<sub>3</sub>N<sub>4</sub>, g-C<sub>3</sub>N<sub>4</sub>/SiO<sub>2</sub> and BP/RP-g-C<sub>3</sub>N<sub>4</sub>/SiO<sub>2</sub> possess a higher N<sub>2</sub> adsorption capacity and pore volume (Table S1†). It was found that the specific surface area of g-C<sub>3</sub>N<sub>4</sub>/SiO<sub>2</sub> (70.291 m<sup>2</sup> g<sup>-1</sup>) and BP/RP-g-C<sub>3</sub>N<sub>4</sub>/SiO<sub>2</sub> (96.603 m<sup>2</sup> g<sup>-1</sup>) was 2.16 times and 2.97 times that of g-C<sub>3</sub>N<sub>4</sub> (32.482 m<sup>2</sup> g<sup>-1</sup>). The larger specific surface area and pore volume provide more adsorption and active sites.

From the FT-IR analysis in Fig. 5a, the broad peak between 2900–3000 cm<sup>-1</sup> is caused by the -NH vibration in the material or the -OH vibration in the absorbed water. The fine characteristic peaks between 1250 and 1680 cm<sup>-1</sup> in g-C<sub>3</sub>N<sub>4</sub>/SiO<sub>2</sub> and BP/RP-g-C<sub>3</sub>N<sub>4</sub>/SiO<sub>2</sub> are the C–N and C=N vibrations of g-C<sub>3</sub>N<sub>4</sub>.<sup>58</sup> The enlarged image of the BP/RP-g-C<sub>3</sub>N<sub>4</sub>/SiO<sub>2</sub> composite is shown in Fig. 5b. The peak at 800 cm<sup>-1</sup> represents the N–H deformation and typical bending vibration of the tris-triazine ring system of g-C<sub>3</sub>N<sub>4</sub>.<sup>59</sup> In composite BP/RP-g-C<sub>3</sub>N<sub>4</sub>/SiO<sub>2</sub>, P–O–C and P=O correspond to the peaks at 904 cm<sup>-1</sup> and 1178 cm<sup>-1</sup>, respectively.<sup>60,61</sup> Noticeably, the appearance of vibrational bands of BP/RP and g-C<sub>3</sub>N<sub>4</sub>/SiO<sub>2</sub> in the BP/RP-g-C<sub>3</sub>N<sub>4</sub>/SiO<sub>2</sub> heterojunctions indicated that BP/RP and g-C<sub>3</sub>N<sub>4</sub>/SiO<sub>2</sub> had been incorporated successfully.

We conducted Raman spectroscopy analysis, shown in Fig. 5c, and found that the hybridization mode of P<sup>0</sup> changed at different values. RP has two distinct peaks in the Raman spectrum at 350.3 cm<sup>-1</sup> and 380.5 cm<sup>-1</sup>, respectively. Then, after RP milling, two new peaks appeared at 445.5 cm<sup>-1</sup> and 466.5 cm<sup>-1</sup>,

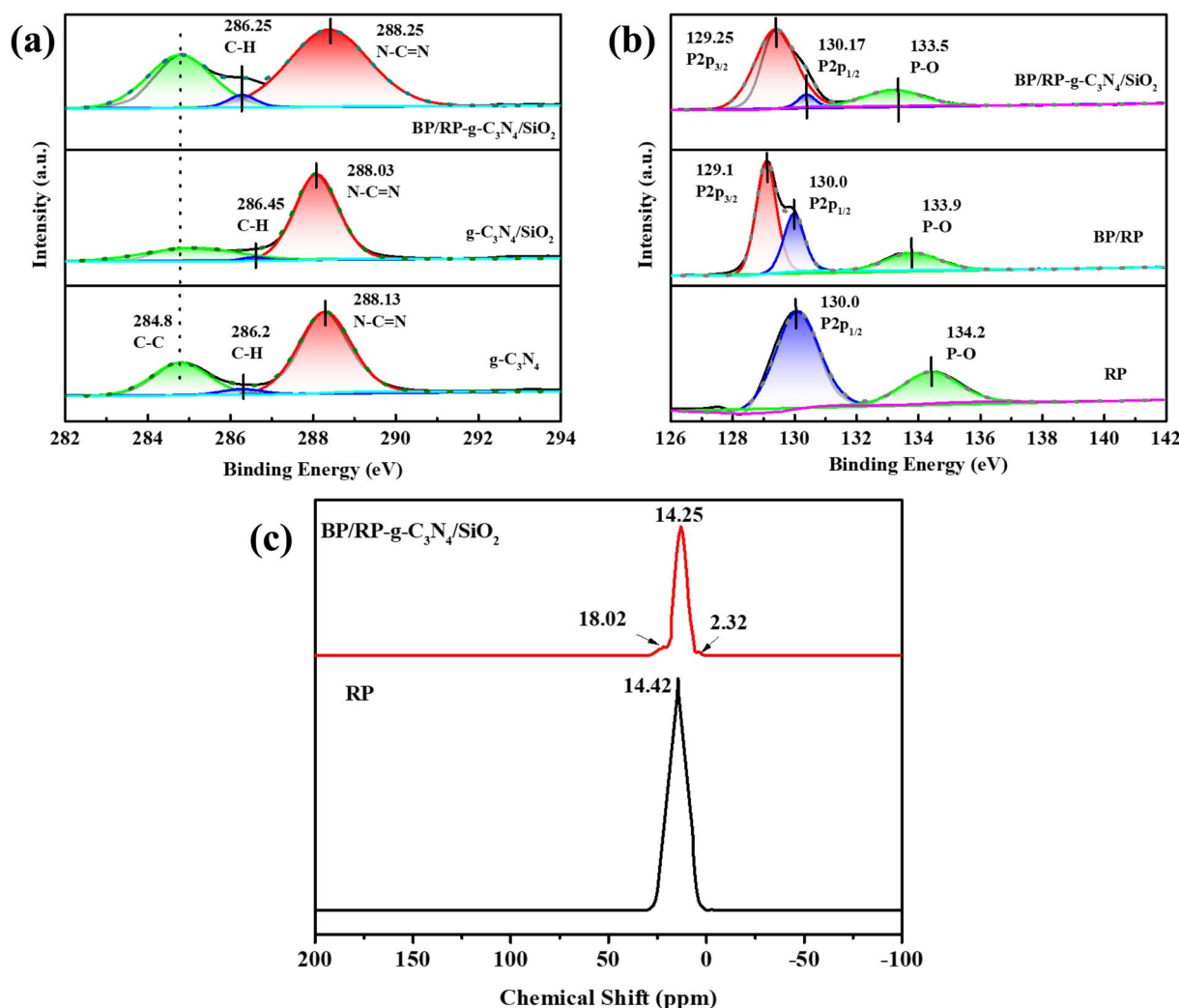


Fig. 6 XPS spectra of (a) C 1s of g-C<sub>3</sub>N<sub>4</sub>, g-C<sub>3</sub>N<sub>4</sub>/SiO<sub>2</sub> and BP/RP-g-C<sub>3</sub>N<sub>4</sub>/SiO<sub>2</sub>, (b) P 2p of RP, BP/RP and BP/RP-g-C<sub>3</sub>N<sub>4</sub>/SiO<sub>2</sub>, (c) solid-state NMR of RP and BP/RP-g-C<sub>3</sub>N<sub>4</sub>/SiO<sub>2</sub>.



which were attributed to the  $B_{2g}$  and  $A_g^2$  patterns of BP, respectively.<sup>62,63</sup> The presence of  $A_g^2$  in BP/RP-g- $C_3N_4/SiO_2$  indicates the generation of BP.<sup>64</sup> In BP/RP-g- $C_3N_4/SiO_2$  (Fig. 5d), the change of D/G indicates that the hybridization mode of C has changed, which is caused by the formation of the P–O–C bond.<sup>65</sup>

The bonding and chemical states of elements in BP/RP-g- $C_3N_4/SiO_2$  were further studied by XPS. In the C spectrum (Fig. 6a), the characteristic peaks at 284.8 eV and 288.13 eV correspond to C–C/C=C and N–C=N bonds in g- $C_3N_4$ , respectively, and the characteristic peak between C–C/C=C and N–C=N is 286.2 eV, corresponding to the C–H bond in g- $C_3N_4$ .<sup>66–68</sup> Compared with g- $C_3N_4$  and g- $C_3N_4/SiO_2$ , the value of the N–C=N bond composite of BP/RP-g- $C_3N_4/SiO_2$  moves to the right, indicating that g- $C_3N_4$  in the composite loses electrons. According to the XPS of RP, BP/RP and BP/RP-g- $C_3N_4/SiO_2$  in Fig. 6b, only a peak value of 130.0 eV and 134.2 eV can be displayed in pure RP. The two weak peaks at 130.0 eV and 133.9 eV in BP/RP represent P 2p<sub>1/2</sub> and the P–O bond, respectively. Among them, 129.1 eV represents the peak value of black phosphorus,<sup>37</sup> thus indicating that our experiment successfully prepared the BP/RP heterostructure, which is consistent with the above characterization results.

In the P 2p spectrum of BP/RP-g- $C_3N_4/SiO_2$ , the characteristic peak at 129.25 eV is caused by P 2p<sub>3/2</sub> of BP, and the characteristic peak at 130.17 eV is P 2p<sub>1/2</sub>.<sup>69</sup> The characteristic peak at

135 eV represents the P–O bond in the BP/RP-g- $C_3N_4/SiO_2$  composite, which lays a foundation for the formation of the P–O–C bond. In the P 2p spectra of RP, BP/RP and BP/RP-g- $C_3N_4/SiO_2$ , the characteristic peaks change between 133 eV and 135 eV. The characteristic peaks of BP/RP-g- $C_3N_4/SiO_2$  in P–O shift to the left by 0.7 eV and 0.4 eV compared with RP and BP/RP, respectively. This shows that BP/RP is gaining electrons in the composite. The formation of P–C bonds by ball milling can be confirmed by <sup>31</sup>P solid-state NMR. As shown in Fig. 6c, the formation of P–C is represented by the feature at 2.32 ppm, and the existence of the BP peak is found at 18.02 ppm. The generation of BP during ball milling is confirmed. Furthermore, compared with RP, BP/RP-g- $C_3N_4/SiO_2$  moves to the right, which is the chemical shift caused by the formation of BP and P–C bonds by RP.<sup>70,71</sup>

### 3.2. Photocatalytic degradation experiment

The variation curve of the RhB concentration ( $C/C_0$ ) with irradiation time ( $t$ ) under visible light irradiation is shown in Fig. 7a. The degradation effect of BP/RP-g- $C_3N_4/SiO_2$  on RhB was the best, which was 90%. The degradation effects of g- $C_3N_4/SiO_2$  and BP/RP on RhB were 51% and 79.3%, respectively. The degradation effect of BP/RP-g- $C_3N_4/SiO_2$  on OFL was the best, which was 85.3%, as shown in Fig. 7b. The degradation effects of g- $C_3N_4/SiO_2$  and BP/RP on OFL were 35.4% and 35.6%, respectively.

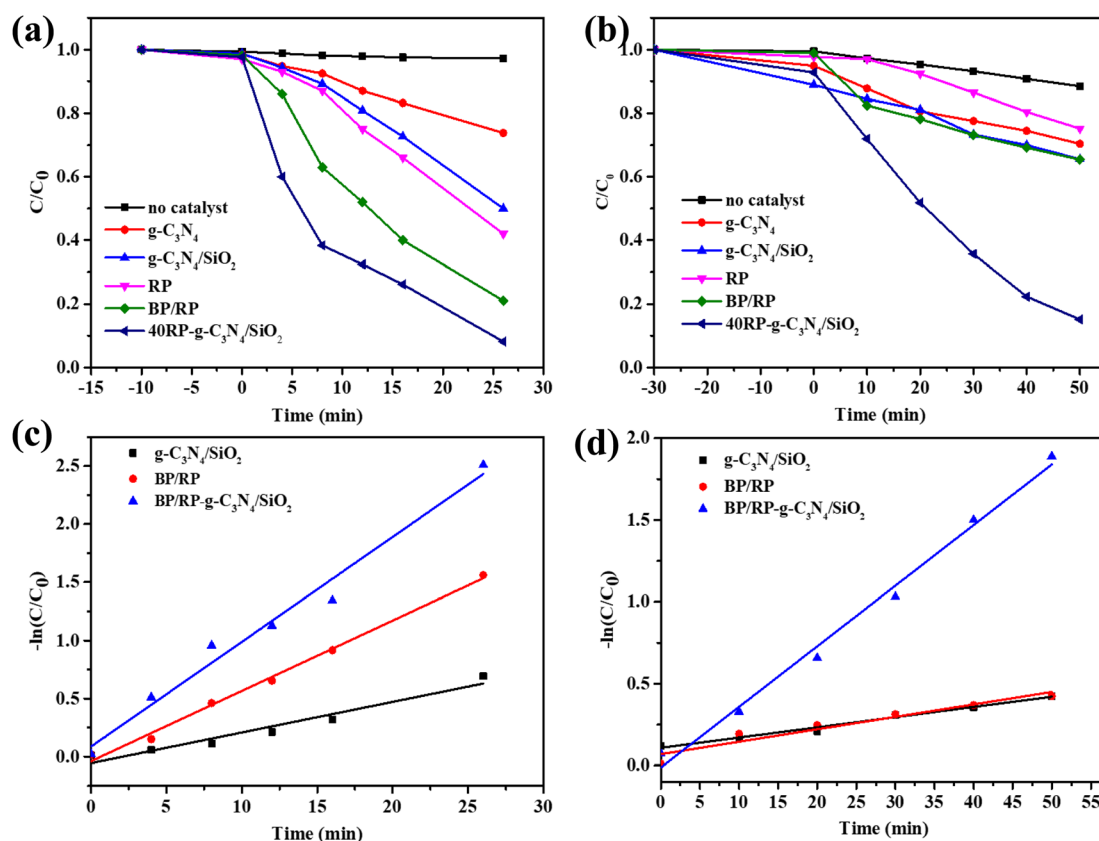


Fig. 7 (a) RhB degradation experiment, (b) OFL degradation experiment, (c) in the pseudo-first-order kinetic curve of RhB, (d) in the pseudo-first-order kinetic curve of OFL.



respectively. In the pseudo-first-order kinetic curve of RhB degradation, the reaction rate of BP/RP-g-C<sub>3</sub>N<sub>4</sub>/SiO<sub>2</sub> is 0.0901 min<sup>-1</sup>, while the reaction rate of g-C<sub>3</sub>N<sub>4</sub>/SiO<sub>2</sub> is 0.0263 min<sup>-1</sup>, and the reaction rate of BP/RP-g-C<sub>3</sub>N<sub>4</sub>/SiO<sub>2</sub> is 3.43 times that of g-C<sub>3</sub>N<sub>4</sub>/SiO<sub>2</sub> (Fig. 7c). In the pseudo-first-order kinetic curve of OFL degradation, the reaction rate of BP/RP-g-C<sub>3</sub>N<sub>4</sub>/SiO<sub>2</sub> is 0.03704 min<sup>-1</sup>, the reaction rate of BP/RP is 0.00761 min<sup>-1</sup>, and the reaction rate of g-C<sub>3</sub>N<sub>4</sub>/SiO<sub>2</sub> is 0.00625 min<sup>-1</sup> (Fig. 7d). The photocatalytic experiment has a better effect on the degradation of RhB than OFL, and the prepared catalyst is more inclined to the degradation of dyes. A total of 2 mg BP/RP-g-C<sub>3</sub>N<sub>4</sub>/SiO<sub>2</sub> can degrade 90% of 60 mg L<sup>-1</sup> RhB in 26 min of illumination, but 5 mg BP/RP-g-C<sub>3</sub>N<sub>4</sub>/SiO<sub>2</sub> can only degrade 85.3% of 20 mg L<sup>-1</sup> OFL in 50 min of illumination. This indicates that in the process of photocatalysis, the chemical reaction between active substances and dyes is stronger, and the prepared catalyst is more practical for dye degradation.

When adding 10%, 20%, 30%, 40%, and 50% RP for ball milling, the mass ratio of SiO<sub>2</sub> in the xRP-g-C<sub>3</sub>N<sub>4</sub>/SiO<sub>2</sub> material is 0.508, 0.451, 0.395, 0.338, and 0.282, respectively. The results showed that the sample containing 200 mg SiO<sub>2</sub> had a better catalytic effect on RhB containing 60 mg L<sup>-1</sup>, and could degrade 51% of the pollutant within 26 min (Fig. S3†). The ball milling time was investigated. The degradation of RhB by adding 40%

RP with a ball milling time of 3 h reached the best value at 66%, and the degradation of RhB by adding 40% RP with a ball milling time of 6 h reached the best value at 86% (Fig. S4†). Among the ball milled samples at 12 h, xRP-g-C<sub>3</sub>N<sub>4</sub>/SiO<sub>2</sub>, 40RP-g-C<sub>3</sub>N<sub>4</sub>/SiO<sub>2</sub> has the best degradation effect on RhB and OFL (Fig. S5†).

Stability and recyclability are extremely important factors that control the practical applicability of catalysts in photocatalysis. Four RhB degradation cycle experiments were carried out, and the results are shown in Fig. 8a. After four cycles, the degradation of RhB by BP/RP-g-C<sub>3</sub>N<sub>4</sub>/SiO<sub>2</sub> reached 85%. After four degradation cycles, the degradation of OFL by BP/RP-g-C<sub>3</sub>N<sub>4</sub>/SiO<sub>2</sub> reached 76% (Fig. 8b). We also observed that there was no obvious change in the color of the sample after the experiment. After four cycles of experiment, there is no significant change in the test Raman results, indicating that the material has good stability (Fig. 8c). In the experiment of degrading RhB, the liquid color changed significantly (Fig. 8d).

### 3.3. Photocatalytic reaction mechanism

It can be seen from UV-vis that the boundary of the absorption spectrum of the composite BP/RP-g-C<sub>3</sub>N<sub>4</sub>/SiO<sub>2</sub> is increasing (Fig. 9a). This shows that there is a strong force between the substances. According to Fig. 9b, the energy gap ( $E_g$ ) width of

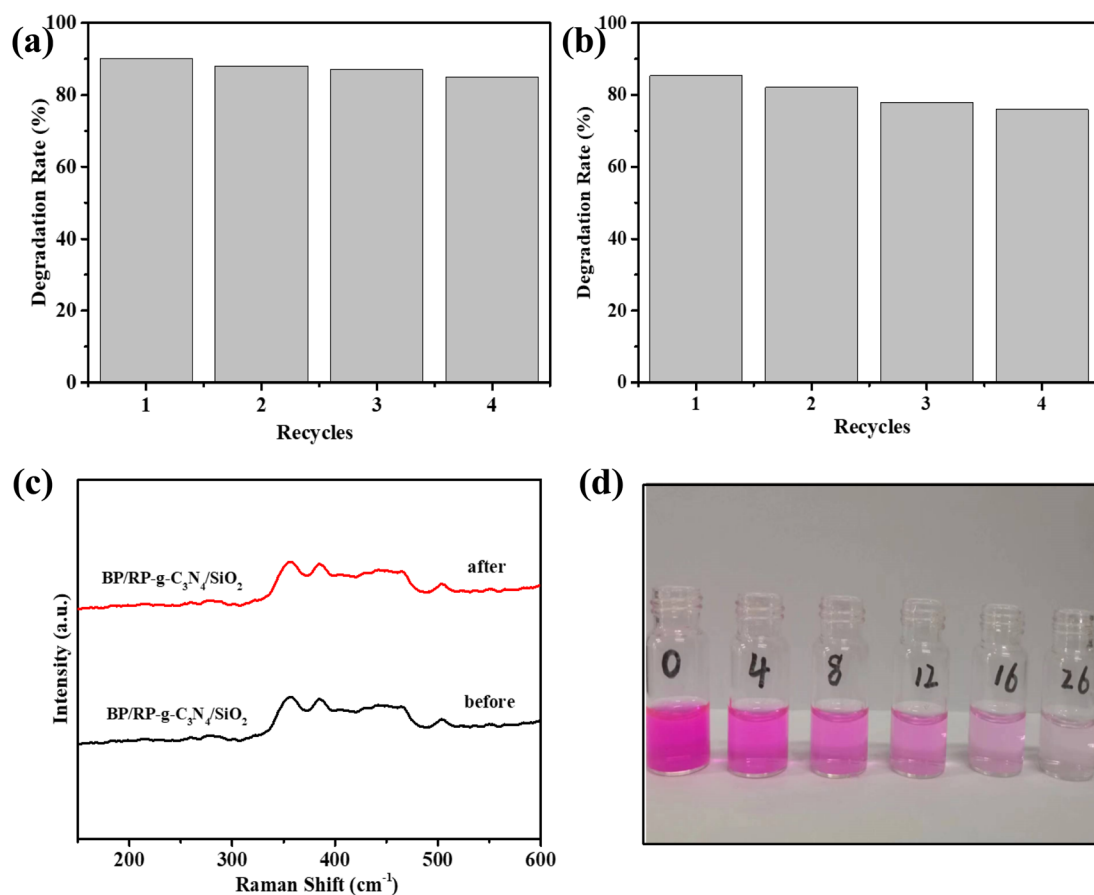


Fig. 8 (a) Degradation RhB cycle experiments, (b) degradation OFL cycle experiments, (c) Raman shift of BP/RP-g-C<sub>3</sub>N<sub>4</sub>/SiO<sub>2</sub> before and after the RhB degradation cycle reaction, (d) the color change of RhB degradation by BP/RP-g-C<sub>3</sub>N<sub>4</sub>/SiO<sub>2</sub>.



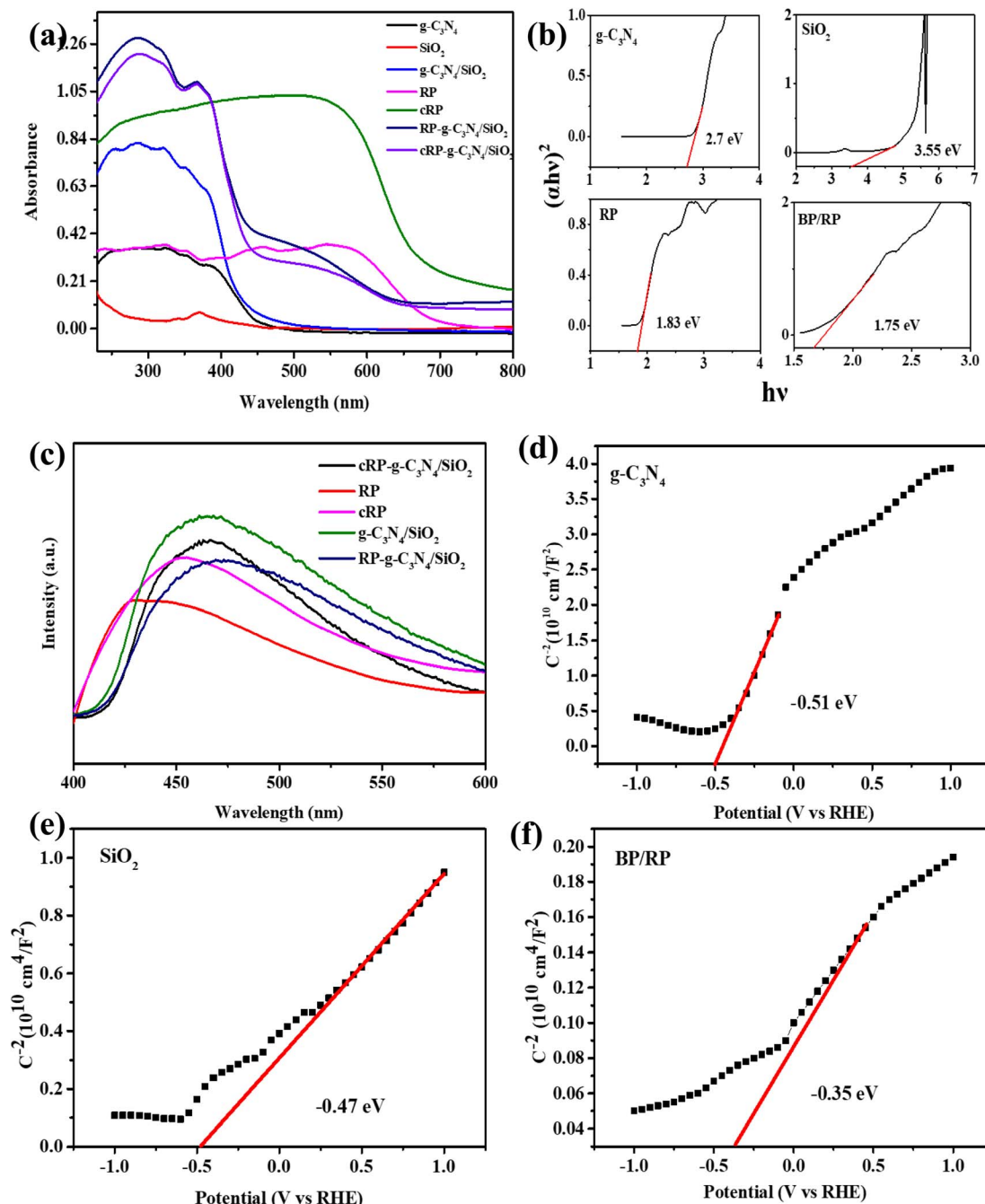


Fig. 9 (a) UV-vis of samples, (b) band gap test of g-C<sub>3</sub>N<sub>4</sub>, SiO<sub>2</sub>, RP and BP/RP, (c) the photoluminescence (PL) spectra of the catalyst sample, (d)–(f) Mott–Schottky plots of g-C<sub>3</sub>N<sub>4</sub>, SiO<sub>2</sub> and BP/RP.

SiO<sub>2</sub> itself is larger, which is 3.55 eV (vs. RHE). When SiO<sub>2</sub> is added to g-C<sub>3</sub>N<sub>4</sub>, the  $E_g$  width of g-C<sub>3</sub>N<sub>4</sub>/SiO<sub>2</sub> becomes smaller from 2.7 eV (vs. RHE) to 2.61 eV (vs. RHE). After ball milling, the  $E_g$  width of RP also decreases from 1.83 eV (vs. RHE) to 1.75 eV (vs. RHE). The final composite BP/RP-g-C<sub>3</sub>N<sub>4</sub>/SiO<sub>2</sub> is 1.6 eV (vs. RHE), and the reason this happens is because the matter forms a heterogeneous structure (Fig. S6<sup>†</sup>). The  $E_g$  of BP/RP-g-C<sub>3</sub>N<sub>4</sub>/SiO<sub>2</sub> is smaller than that of g-C<sub>3</sub>N<sub>4</sub>, SiO<sub>2</sub> and RP, indicating that the material can promote the transfer of electrons and holes

more quickly, and promotes the formation of more active substances.

The photoluminescence (PL) spectra of all samples are shown in Fig. 9c. The PL intensity of BP/RP-g-C<sub>3</sub>N<sub>4</sub>/SiO<sub>2</sub> can be intuitively seen to be lower than that of other catalyst samples, indicating that partial relaxation of BP/RP-g-C<sub>3</sub>N<sub>4</sub>/SiO<sub>2</sub> excitons may occur through charge transfer of electrons and holes, rather than through radiation paths.<sup>72,73</sup> Thus, it can be inferred that BP/RP-g-C<sub>3</sub>N<sub>4</sub>/SiO<sub>2</sub> photogenerated carriers can prolong



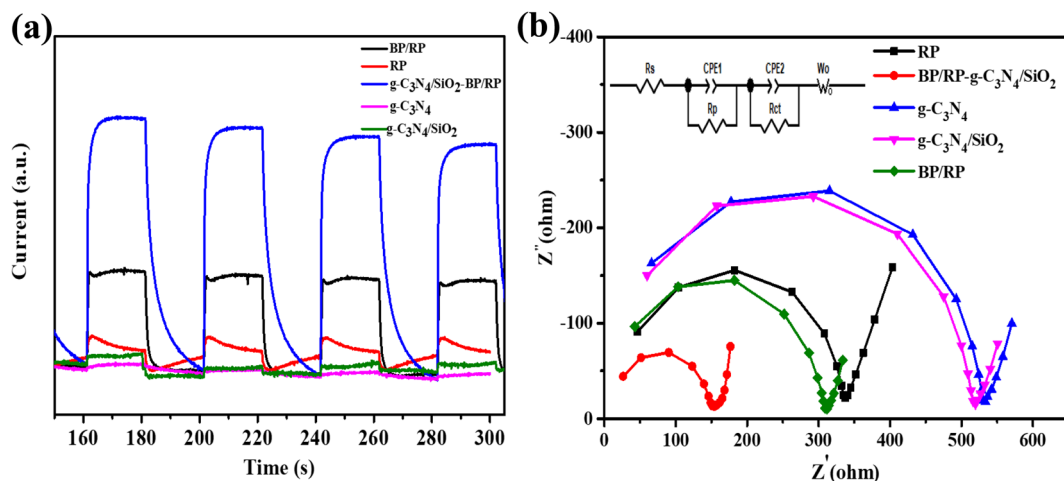


Fig. 10 (a)  $I-t$  responses and (b) EIS of RP, BP/RP,  $g-C_3N_4$ ,  $g-C_3N_4/SiO_2$  and BP/RP- $g-C_3N_4/SiO_2$ .

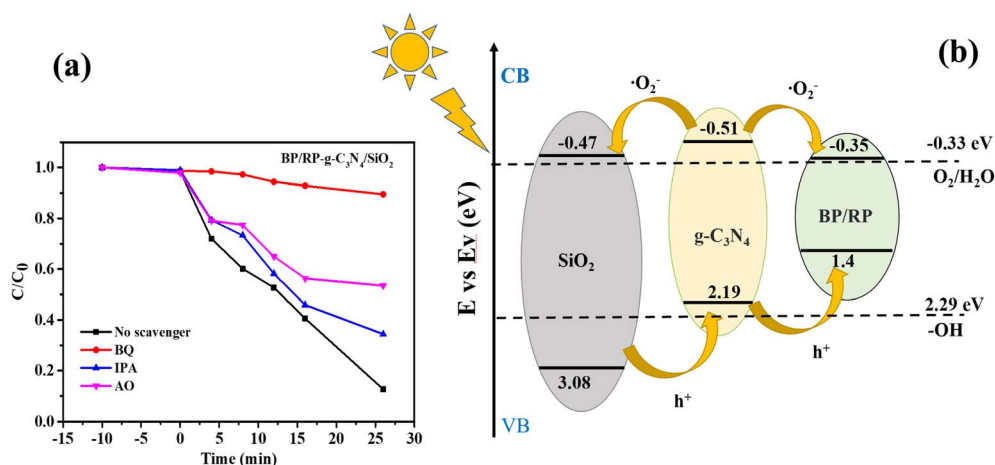


Fig. 11 (a) BP/RP- $g-C_3N_4/SiO_2$  degradation RhB active substance capture experiment. (b) The photocatalytic mechanism of BP/RP- $g-C_3N_4/SiO_2$ .

their service life and enhance the degradation effect compared with others.

Meanwhile, the conduction band gap width ( $E_{CB}$ ) of each material can be obtained by producing a Mott-Schottky curve (Fig. 9d-f). During the test, the conduction band values of the three monomers were measured compared with the reversible hydrogen electrode. The conduction band gap widths ( $E_{CB}$ ) of  $g-C_3N_4$ ,  $SiO_2$ , BP/RP and BP/RP- $g-C_3N_4/SiO_2$  are  $-0.51$  eV,  $-0.47$  eV,  $-0.35$  eV and  $-0.65$  eV, respectively (Fig. S6<sup>†</sup>). In addition, the conduction bands ( $E_{VB}$ ) of  $g-C_3N_4$ ,  $SiO_2$ , BP/RP and BP/RP- $g-C_3N_4/SiO_2$  are  $2.19$  eV,  $3.08$  eV,  $1.4$  eV and  $0.95$  eV, respectively, based on the formula below:<sup>74,75</sup>

$$E_{CB} = E_{VB} - E_g$$

According to the corresponding conditions of the photocurrent, we can clearly see that under the simulated sunlight of  $350$  W, the photocurrent response current of BP/RP- $g-C_3N_4/SiO_2$

is the largest, and the photocurrent response current of  $g-C_3N_4$  is the smallest. Furthermore, the current generated by BP/RP- $g-C_3N_4/SiO_2$  is about 70 times stronger than that of  $g-C_3N_4$  (Fig. 10a). This is understandable because the heterostructures are formed in the composites, which facilitate the transfer of electrons and holes and inhibit their recombination, indicating that the heterojunction was successfully prepared between the P atom and  $g-C_3N_4/SiO_2$ .

In Fig. 10b, the charge transfer of photocatalytic materials is revealed by the equivalent circuit diagram of electrochemical impedance spectroscopy (EIS).<sup>76</sup> The radius of the arc usually indicates the resistance of electron transport at the interface. A smaller radius means more rapid charge transfer.<sup>76,77</sup> According to the EIS, the radius of BP/RP- $g-C_3N_4/SiO_2$  is the smallest, while that of  $g-C_3N_4$  is the largest, which is consistent with the above photocurrent response results.

In the degradation of RhB, the active substances in the BP/RP- $g-C_3N_4/SiO_2$  system were determined by scavenger experiment. In the quenching experiment, isopropanol (IPA), 4-



benzoquinone (BQ) and ammonium oxalate (AO) were used as quenching agents of the hydroxyl radical ( $^{\bullet}\text{OH}$ ), superoxide radical ( $^{\bullet}\text{O}_2^-$ ) and hole ( $h^+$ ) in the RhB degradation, respectively. In the  $g\text{-C}_3\text{N}_4/\text{SiO}_2$  degradation of RhB, it can be seen that  $^{\bullet}\text{O}_2^-$  dominates the degradation process, which can inhibit the degradation of pollutants by up to 30%, indicating that  $^{\bullet}\text{O}_2^-$  is the main active substance in this case, and the inhibitory effect of  $h^+$  is stronger than that of  $^{\bullet}\text{OH}$  (Fig. S7†). In the BP/RP degradation of RhB, it was found that the same active substance  $^{\bullet}\text{O}_2^-$  played a role in catalysis, but the role of  $^{\bullet}\text{OH}$  was stronger than that of  $h^+$  (Fig. S8†). In composite materials BP/RP- $g\text{-C}_3\text{N}_4/\text{SiO}_2$ ,  $^{\bullet}\text{O}_2^-$  significantly inhibits the degradation of pollutants, and only 10% of pollutants are degraded, indicating that  $^{\bullet}\text{O}_2^-$  is still dominant (Fig. 11a). On the whole,  $^{\bullet}\text{O}_2^-$  is the main active substance to degrade RhB, and the degradation mechanism of BP/RP- $g\text{-C}_3\text{N}_4/\text{SiO}_2$  is similar to that of  $g\text{-C}_3\text{N}_4/\text{SiO}_2$ , but different from that of BP/RP.

According to the most relevant literature, the CB and VB values of BP/RP meet the requirements. Depending on the band structures of  $g\text{-C}_3\text{N}_4$ ,  $\text{SiO}_2$ ,  $g\text{-C}_3\text{N}_4/\text{SiO}_2$ , BP/RP and RP, it can be speculated that BP/RP- $g\text{-C}_3\text{N}_4/\text{SiO}_2$  composites contain type I and type II heterostructures.

$g\text{-C}_3\text{N}_4$  and BP/RP were excited under simulated sunlight to produce photogenic charge carriers. The  $e^-$  in the VB was transferred to the CB, and left  $h^+$  in the VB. In  $g\text{-C}_3\text{N}_4/\text{SiO}_2$ , the CB position of  $g\text{-C}_3\text{N}_4$  is more negative than that of  $\text{SiO}_2$ , and the VB position of  $\text{SiO}_2$  is more positive than that of  $g\text{-C}_3\text{N}_4$ . The  $e^-$  in the CB of  $g\text{-C}_3\text{N}_4$  could rapidly transfer to the CB of  $\text{SiO}_2$ . In the meanwhile, the  $h^+$  in the VB of  $\text{SiO}_2$  could swiftly move to the VB of  $g\text{-C}_3\text{N}_4$ . Moreover, the CB position of  $g\text{-C}_3\text{N}_4$  is more negative than that of BP/RP. The  $e^-$  in the CB of  $g\text{-C}_3\text{N}_4$  could swiftly move to the CB of BP/RP. The CB potential of  $g\text{-C}_3\text{N}_4$  is more negative than that of  $^{\bullet}\text{O}_2^-$  ( $-0.33$  eV). This situation tends to produce  $^{\bullet}\text{O}_2^-$ . However, the VB potential of  $\text{SiO}_2$  is more positive than that of  $\text{OH}^-/\text{OH}$  ( $+2.27$  eV), and  $h^+$  in the VB of BP/RP could not oxidize  $\text{H}_2\text{O}$  and  $\text{OH}^-$  to form  $^{\bullet}\text{OH}$ . The  $^{\bullet}\text{O}_2^-$  and  $h^+$  could oxidize RhB directly. Thus, the heterostructure mechanism of the BP/RP- $g\text{-C}_3\text{N}_4/\text{SiO}_2$  composites is proposed in Fig. 11b.

## 4. Conclusion

In conclusion, a one-step ball-milling method was successfully used to achieve the BP/RP- $g\text{-C}_3\text{N}_4/\text{SiO}_2$  multi-heterojunction. The existence of BP and the formation of P-C bonds in BP/RP- $g\text{-C}_3\text{N}_4/\text{SiO}_2$  were confirmed by NMR. The degradation performance of BP/RP- $g\text{-C}_3\text{N}_4/\text{SiO}_2$  was superior compared to those of  $g\text{-C}_3\text{N}_4$  and  $\text{SiO}_2/g\text{-C}_3\text{N}_4$ . The RhB removal efficiency of BP/RP- $g\text{-C}_3\text{N}_4/\text{SiO}_2$  reached 90%, which is 1.8 times greater than that of the  $g\text{-C}_3\text{N}_4/\text{SiO}_2$  sample. The degradation of OFL by BP/RP- $g\text{-C}_3\text{N}_4/\text{SiO}_2$  is 3.41 times greater than that of the  $g\text{-C}_3\text{N}_4/\text{SiO}_2$  sample. In addition, the BP/RP- $g\text{-C}_3\text{N}_4/\text{SiO}_2$  revealed distinguished stability of the catalyst and recyclability for practical applications in the process of degradation of RhB and OFL. The current work displays the potential of using carbon-based materials for environmental purification, particularly in removing dye from wastewater.

## Data availability

Data will be made available upon request to the corresponding author.

## Author contributions

Jiancheng Li: investigation, resources, writing—original draft, and visualization. Chi Wang: writing—review and editing, visualization, supervision. Yixing Ma: writing—review and editing. Kai Li: visualization and supervision. Yi Mei: supervision.

## Conflicts of interest

The authors have no relevant financial or non-financial interests to disclose.

## Acknowledgements

This study was financially supported by the National Natural Science Foundation of China (52260013, 22068019).

## References

- 1 K. A. Adegoke, M. Iqbal, H. Louis and O. S. Bello, Synthesis, characterization and application of CdS/ZnO nanorod heterostructure for the photodegradation of Rhodamine B dye, *Mater. Sci. Energy Technol.*, 2019, **2**, 329–336.
- 2 J. W. Peterson, B. Gu and M. D. Seymour, Surface interactions and degradation of a fluoroquinolone antibiotic in the dark in aqueous  $\text{TiO}_2$  suspensions, *Sci. Total Environ.*, 2015, **532**, 398–403.
- 3 J. Wang and S. Wang, Removal of pharmaceuticals and personal care products (PPCPs) from wastewater: A review, *J. Environ. Manage.*, 2016, **182**, 620–640.
- 4 J. Wang, R. Zhuan and L. Chu, The occurrence, distribution and degradation of antibiotics by ionizing radiation: An overview, *Sci. Total Environ.*, 2019, **646**, 1385–1397.
- 5 H. Li, W. Zhang and Y. Liu, HZSM-5 zeolite supported boron-doped  $\text{TiO}_2$  for photocatalytic degradation of ofloxacin, *J. Mater. Res. Technol.*, 2020, **9**, 2557–2567.
- 6 P. Chen, L. Blaney and G. Cagnetta, Degradation of Ofloxacin by Perylene Diimide Supramolecular Nanofiber Sunlight-Driven Photocatalysis, *Environ. Sci. Technol.*, 2019, **3**, 1564–1575.
- 7 T. Senasu, T. Narenuch, K. Wannakam, T. Chankhanittha and S. Nanan, Solvothermally grown BiOCl catalyst for photodegradation of cationic dye and fluoroquinolone-based antibiotics, *J. Mater. Sci.: Mater. Electron.*, 2020, **31**, 9685–9694.
- 8 R. Anjali and S. Shanthakumar, Insights on the current status of occurrence and removal of antibiotics in wastewater by advanced oxidation processes, *J. Environ. Manage.*, 2019, **246**, 51–62.
- 9 B. L. Phoon, C. C. Ong, M. S. Mohamed Saheed, P. L. Show, J. S. Chang, T. C. Ling, S. S. Lam and J. C. Juan, Conventional



- and emerging technologies for removal of antibiotics from wastewater, *J. Hazard. Mater.*, 2020, **400**, 122961.
- 10 I. Arslan-Alaton, A. Karatas, Ö. Pehlivan, O. Koba Uzun and T. Ölmez-Hancı, Effect of UV-A-assisted iron-based and UV-C-driven oxidation processes on organic matter and antibiotic resistance removal in tertiary treated urban wastewater, *Catal. Today*, 2021, **361**, 152–158.
  - 11 M. J. F. Calvete, G. Piccirillo, C. S. Vinagreiro and M. M. Pereira, Hybrid materials for heterogeneous photocatalytic degradation of antibiotics, *Coord. Chem. Rev.*, 2019, **395**, 63–85.
  - 12 Y. Sun, D. W. Cho, N. J. D. Graham, D. Hou, A. C. K. Yip, E. Khan, H. Song, Y. Li and D. C. W. Tsang, Degradation of antibiotics by modified vacuum-UV based processes: Mechanistic consequences of H<sub>2</sub>O<sub>2</sub> and K<sub>2</sub>S<sub>2</sub>O<sub>8</sub> in the presence of halide ions, *Sci. Total Environ.*, 2019, **664**, 312–321.
  - 13 V. B. Lima, L. A. Goulart, R. S. Rocha, J. R. Steter and M. R. V. Lanza, Degradation of antibiotic ciprofloxacin by different AOP systems using electrochemically generated hydrogen peroxide, *Chemosphere*, 2020, **247**, 125807.
  - 14 E. A. Serna-Galvis, D. Montoya-Rodríguez, L. Isaza-Pineda, M. Ibáñez, F. Hernández, A. Moncayo-Lasso and R. A. Torres-Palma, Sonochemical degradation of antibiotics from representative classes-Considerations on structural effects, initial transformation products, antimicrobial activity and matrix, *Ultrason. Sonochem.*, 2019, **50**, 157–165.
  - 15 A. Muniyasamy, G. Sivaporul, A. Gopinath, R. Lakshmanan, A. Altaee, A. Achary and P. Velayudhaperumal Chellam, Process development for the degradation of textile azo dyes (mono-, di-, poly-) by advanced oxidation process -Ozonation: Experimental & partial derivative modelling approach, *J. Environ. Manage.*, 2020, **265**, 110397.
  - 16 M. Tariq, M. Muhammad, J. Khan, A. Raziq, M. K. Uddin, A. Niaz, S. S. Ahmed and A. Rahim, Removal of Rhodamine B dye from aqueous solutions using photo-Fenton processes and novel Ni-Cu@MWCNTs photocatalyst, *J. Mol. Liq.*, 2020, **312**, 113399.
  - 17 S. Chakma, L. Das and V. S. Moholkar, Dye decolorization with hybrid advanced oxidation processes comprising sonolysis/Fenton-like/photo-ferrioxalate systems: A mechanistic investigation, *Sep. Purif. Technol.*, 2015, **156**, 596–607.
  - 18 X. Ding, L. Gutierrez, J. P. Croue, M. Li, L. Wang and Y. Wang, Hydroxyl and sulfate radical-based oxidation of RhB dye in UV/H<sub>2</sub>O<sub>2</sub> and UV/persulfate systems: Kinetics, mechanisms, and comparison, *Chemosphere*, 2020, **253**, 126655.
  - 19 P. V. Gayathri, S. Yesodharan and E. P. Yesodharan, Microwave/Persulfate assisted ZnO mediated photocatalysis (MW/PS/UV/ZnO) as an efficient advanced oxidation process for the removal of RhB dye pollutant from water, *J. Environ. Chem. Eng.*, 2019, **7**, 103122.
  - 20 N. Phutanon, P. Pisitsak, H. Manuspiya and S. Ummartyotin, Synthesis of three dimensional hierarchical CuO flower-like architecture and its photocatalytic activity for rhodamine b degradation, *J. Sci.: Adv. Mater. Devices*, 2018, **3**, 310–316.
  - 21 Y. Zhou, M. Yu, H. Liang, J. Chen, L. Xu and J. Niu, Novel dual-effective Z-scheme heterojunction with g-C<sub>3</sub>N<sub>4</sub>, Ti<sub>3</sub>C<sub>2</sub> MXene and black phosphorus for improving visible light-induced degradation of ciprofloxacin, *Appl. Catal., B*, 2021, **291**, 120105.
  - 22 Y. Deng, L. Tang, C. Feng, G. Zeng, J. Wang, Y. Zhou, Y. Liu, B. Peng and H. Feng, Construction of plasmonic Ag modified phosphorous-doped ultrathin g-C<sub>3</sub>N<sub>4</sub> nanosheets/BiVO<sub>4</sub> photocatalyst with enhanced visible-near-infrared response ability for ciprofloxacin degradation, *J. Hazard. Mater.*, 2018, **344**, 758–769.
  - 23 J. Fu, J. Yu, C. Jiang and B. Cheng, g-C<sub>3</sub>N<sub>4</sub>-based heterostructured photocatalysts, *Adv. Energy Mater.*, 2017, **8**, 1701503.
  - 24 G. Peng, L. Xing, J. Barrio, M. Volokh and M. Shalom, A general synthesis of porous carbon nitride films with tunable surface area and photophysical properties, *Angew. Chem., Int. Ed.*, 2018, **57**, 1186–1192.
  - 25 C. Zhou, C. Lai, D. Huang, G. Zeng, C. Zhang, M. Cheng, L. Hu, J. Wan, W. Xiong, M. Wen, X. Wen and L. Qin, Highly porous carbon nitride by supramolecular preassembly of monomers for photocatalytic removal of sulfamethazine under visible light driven, *Appl. Catal., B*, 2018, **220**, 202–210.
  - 26 Y. Song, J. Tian, S. Gao, P. Shao, J. Qi and F. Cui, Photodegradation of sulfonamides by g-C<sub>3</sub>N<sub>4</sub> under visible light irradiation: Effectiveness, mechanism and pathways, *Appl. Catal., B*, 2017, **210**, 88–96.
  - 27 S. Naraginti, Y. Yu, Z. Fang and Y. Yong, Novel tetrahedral Ag<sub>3</sub>PO<sub>4</sub>/N-rGO for photocatalytic detoxification of sulfamethoxazole: Process optimization, transformation pathways and biotoxicity assessment, *Chem. Eng. J.*, 2019, **375**, 122035.
  - 28 Y. Shiraishi, Y. Kofuji and S. Kanazawa, Platinum nanoparticles strongly associated with graphitic carbon nitride as efficient co-catalysts for photocatalytic hydrogen evolution under visible light, *Chem. Commun.*, 2014, **96**, 15255.
  - 29 P. Zhu and Z. Ren, Mesoporous Phosphorus-Doped g-C<sub>3</sub>N<sub>4</sub> Nanostructured Flowers with Superior Photocatalytic Hydrogen Evolution Performance, *ACS Appl. Mater. Interfaces*, 2015, **30**, 16850.
  - 30 X. Bai, L. Wang and Y. Wang, Enhanced oxidation ability of g-C<sub>3</sub>N<sub>4</sub> photocatalytic via C<sub>60</sub> modification, *Appl. Catal., B*, 2014, **152–153**, 262–270.
  - 31 K. Wang, G. Zhang, J. Li, Y. Li and X. Wu, 0D/2D Z-Scheme heterojunctions of bismuth tantalate quantum dots/ultrathin g-C<sub>3</sub>N<sub>4</sub> nanosheets for highly efficient visible light photocatalytic degradation of antibiotics, *ACS Appl. Mater. Interfaces*, 2017, **9**, 43704–43715.
  - 32 M. Dan, J. Xiang, F. Wu, S. Yu, Q. Cai, L. Ye, Y. Ye and Y. Zhou, Rich active-edge-site MoS<sub>2</sub> anchored on reduction sites in metal sulfide heterostructure: toward robust visible light photocatalytic hydrogen sulphide splitting, *Appl. Catal., B*, 2019, **256**, 117870.



- 33 Q. Zhao, J. Wang, Z. Li, Y. Guo, J. Wang, B. Tang, A. Abudula and G. Guan, Heterostructured graphitic-carbon-nitride-nanosheets/copper (I) oxide composite as an enhanced visible light photocatalyst for decomposition of tetracycline antibiotics, *Sep. Purif. Technol.*, 2020, **250**, 117238.
- 34 T. H. Chiang and T. E. Hsieh, Int. A study of monomer's effect on adhesion strength of UV-curable resins, *Adhes*, 2006, **26**, 520–531.
- 35 K. Yoshinaga, Y. Tani and Y. Tanaka, Surface modification of fine colloidal silica with copolymer silane-coupling agents composed of maleic anhydride, *Colloid Polym. Sci.*, 2002, **280**, 85–89.
- 36 H. Qiang, X. Niu, C. Nong, S. Hua, W. Zui, J. Gao and W. Yang, A highly efficient g-C<sub>3</sub>N<sub>4</sub>/SiO<sub>2</sub> heterojunction: the role of SiO<sub>2</sub> in the enhancement of visible light photocatalytic activity, *Phys. Chem. Chem. Phys.*, 2016, **18**, 31410.
- 37 Y. Q. Wang, J. K. Wu, Y. Yan, L. Li, P. Lu, J. N. Guan, N. Lu and X. Yuan, Black phosphorus-based semiconductor multi-heterojunction TiO<sub>2</sub>-BiVO<sub>4</sub>-BP/RP film with an in situ junction and Z-scheme system for enhanced photoelectrocatalytic activity, *Chem. Eng. J.*, 2021, **403**, 126313.
- 38 G. M. Xu, C. Ma, J. J. Wei, X. Yang, T. T. Wang, C. Tan, K. H. Yang, K. N. Jiang, G. L. Yue, C. Zhang and X. Li, Enhanced photocatalytic activity of 3D hierarchical RP/BP/BiOOH via oxygen vacancies and double heterojunctions, *Chemosphere*, 2022, **300**, 134485.
- 39 H. Yuan, Y. Zhao, Y. Wang, J. Duan, B. He and Q. Tang, Sonochemistry-assisted black/red phosphorus hybrid quantum dots for dye-sensitized solar cells, *J. Power Sources*, 2019, **410–411**, 53–58.
- 40 T. Sakthivel, X. Y. Huang, Y. C. Wu and S. Rtimi, Recent progress in black phosphorus nanostructures as environmental photocatalysts, *Chem. Eng. J.*, 2020, **379**, 122297.
- 41 Z. Y. Song, Y. Ma and J. S. Ye, J. Preparation of stable black phosphorus nanosheets and their electrochemical catalytic study, *Electroanal. Chem.*, 2020, **856**, 113595.
- 42 D. Y. Qiu, F. H. D. Jornada and S. G. Louie, Environmental Screening Effects in 2D Materials: Renormalization of the Bandgap, Electronic Structure, and Optical Spectra, of Few-Layer Black Phosphorus, *Nano Lett.*, 2017, **17**, 4706–4712.
- 43 J. H. Wang, D. N. Liu, H. Huang, N. Yang, B. Yu, M. Wen and X. Wang, In-Plane Black Phosphorus/Dicobalt Phosphide Heterostructure for Efficient Electrocatalysis, *Angew. Chem., Int. Ed.*, 2018, **57**(10), 2600–2604.
- 44 S. T. Li, Y. H. Zhang and H. W. Huang, Black phosphorus-based heterostructures for photocatalysis and photoelectrochemical water splitting, *J. Energy Chem.*, 2022, **67**, 745–779.
- 45 M. S. Zhu, S. Kim, L. Mao, J. Y. Zhang and X. C. Wang, Metal-Free Photocatalyst for H<sub>2</sub> Evolution in Visible to Near-Infrared Region: Black Phosphorus/Graphitic Carbon Nitride, *J. Am. Chem. Soc.*, 2017, **37**, 13234–13242.
- 46 Z. Eroglu, M. S. Ozer, T. Kubanaliev and H. Kili, Synergism between few-layer black phosphorus and graphitic carbon nitride enhances the photo-redox C-H arylation under visible light irradiation, *Catal. Sci. Technol.*, 2022, **12**, 5379–5389.
- 47 D. Y. He, Z. C. Zhang, Y. Xing, Y. J. Zhou and H. Yang, Black phosphorus/graphitic carbon nitride: A metal-free photocatalyst for “green” photocatalytic bacterial inactivation under visible light, *Chem. Eng. J.*, 2020, **384**, 123258.
- 48 Z. Q. Li, P. Song, Z. X. Yang and Q. Wang, In situ formation of one-dimensional CoMoO<sub>4</sub>/MoO<sub>3</sub> heterojunction as an effective trimethylamine gas sensor, *Ceram. Int.*, 2018, **44**, 3364–3370.
- 49 L. Peng, Z. W. Li, R. R. Zheng, H. Yu and X. T. Dong, Preparation and characterization of mesoporous g-C<sub>3</sub>N<sub>4</sub>/SiO<sub>2</sub> material with enhanced photocatalytic activity, *J. Mater. Sci.*, 2019, **113**, 1785–1794.
- 50 Y. Shiraishi, S. Kanazawa and Y. Sugano, Highly selective production of hydrogen peroxide on graphitic carbon nitride (g-C<sub>3</sub>N<sub>4</sub>) photocatalyst activated by visible light, *ACS Catal.*, 2014, **4**, 774.
- 51 Y. Li, H. Zhang and P. Liu, Cross-Linked g-C<sub>3</sub>N<sub>4</sub>/rGO nanocomposites with tunable band structure and enhanced visible light photocatalytic activity, *Small*, 2013, **9**, 3336.
- 52 Z. P. Ren, D. H. Liu, Q. Xue, J. J. Li, Y. W. Sun, R. Q. Zhang, Y. P. Zhai and Y. G. Liu, Facile fabrication nano-sized red phosphorus with enhanced photocatalytic activity by hydrothermal and ultrasonic method, *Catal. Today*, 2020, **340**, 115–120.
- 53 Q. Hao, X. Niu, C. Nie and S. Hao, A highly efficient g-C<sub>3</sub>N<sub>4</sub>/SiO<sub>2</sub> heterojunction: the role of SiO<sub>2</sub> in the enhancement of visible light photocatalytic activity, *Phys. Chem. Chem. Phys.*, 2016, **18**, 31410.
- 54 S. Zhu, S. Shou, W. Wan, L. Jian, L. Zhi and C. Jimmy, A black-red phosphorus heterostructure for efficient visible-light-driven photocatalysis, *J. Mater. Chem. A*, 2015, **3**, 3285.
- 55 S. Li, S. Hu, W. Jiang, Y. Liu, Y. Zhou, J. Liu and Z. Wang, Facile synthesis of cerium oxide nanoparticles decorated flower-like bismuth molybdate for enhanced photocatalytic activity toward organic pollutant degradation, *J. Colloid Interface Sci.*, 2018, **530**, 171–178.
- 56 S. Li, S. Hu, W. Jiang, Y. Liu, Y. Zhou, Y. Liu and L. Mo, Hierarchical architectures of bismuth molybdate nanosheets onto nickel titanate nanofibers: Facile synthesis and efficient photocatalytic removal of tetracycline hydrochloride, *J. Colloid Interface Sci.*, 2018, **521**, 42–49.
- 57 D. Wang, H. Shen, L. Guo, C. Wang and F. Fu, Porous BiOBr/Bi<sub>2</sub>MoO<sub>6</sub> Heterostructures for Highly Selective Adsorption of Methylene Blue, *ACS Omega*, 2016, **1**, 566–577.
- 58 J. S. Hu, P. F. Zhang, W. J. An, L. L. Ying and H. Liang, In-situ Fe-doped g-C<sub>3</sub>N<sub>4</sub> heterogeneous catalyst via photocatalysis-Fenton reaction with enriched photocatalytic performance for removal of complex wastewater, *Appl. Catal., B*, 2019, **245**, 130–142.
- 59 Y. G. Ma, J. Li, E. Z. Liu, J. Wan, X. Y. Hu and J. Fan, High efficiency for H<sub>2</sub> evolution and NO removal over the Ag



- nanoparticles bridged g-C<sub>3</sub>N<sub>4</sub> and WS<sub>2</sub> heterojunction photocatalysts, *Appl. Catal., B*, 2017, **219**, 467–478.
- 60 K. K. Bai, J. C. Fan, P. H. Shi, Y. L. Min and Q. J. Xu, Directly ball milling red phosphorus and expanded graphite for oxygen evolution reaction, *J. Power Sources*, 2020, **456**, 228003.
- 61 Z. X. Yu, J. X. Song, M. L. Gordin, R. Yi, D. H. Tang and D. H. Wang, Phosphorus-Graphene Nanosheet Hybrids as Lithium-Ion Anode with Exceptional High-Temperature Cycling Stability, *Adv. Sci.*, 2015, **2**, 1400020.
- 62 R. Boppella, W. Yang, J. Tan, H. C. Kwon, J. Park and J. Moon, Black phosphorus supported Ni<sub>2</sub>P co-catalyst on graphitic carbon nitride enabling simultaneous boosting charge separation and surface reaction, *Appl. Catal., B*, 2019, **242**, 422–430.
- 63 X. Huang, P. Sheng, Z. Tu, F. Zhang, J. Wang, H. Geng, Y. Zou, C. Di, Y. Yi, Y. Sun, W. Xu and D. Zhu, A two-dimensional  $\pi$ -d conjugated coordination polymer with extremely high electrical conductivity and ambipolar transport behaviour, *Nat. Commun.*, 2015, **6**, 7408.
- 64 G. C. Liu, Q. Hui, Z. Y. Hui, S. W. Liu, Y. Jin, Y. D. Liu and Q. Xiang, Black/red phosphorus Z-scheme hybrid with novel photosynthesis-inspired electrolyte additives for enhanced photoelectrochemical activity, *Opt. Mater.*, 2021, **114**, 110934.
- 65 X. J. Yang, T. F. Liu, M. Zhang, B. Song, Q. Y. Li and J. J. Yang, Interfacial dual vacancies modulating electronic structure to promote the separation of photogenerated carriers for efficient CO<sub>2</sub> photoreduction, *Appl. Surf. Sci.*, 2021, **551**, 149345.
- 66 S. H. Li, N. Zhang, X. Q. Xie and R. Luque, Stress-Transfer-Induced In Situ Formation of Ultrathin Nickel Phosphide Nanosheets for Efficient Hydrogen, *Angew. Chem., Int. Ed.*, 2018, **57**, 13082–13085.
- 67 C. C. Wang, X. D. Dua, J. Li, X. X. Guo, P. Wang and J. Zhang, Photocatalytic Cr (VI) reduction in metal-organic frameworks: A mini-review, *Appl. Catal., B*, 2016, **193**, 198–216.
- 68 X. Wang, M. Z. Hong, F. W. Zhang, Z. Y. Zhuang and Y. Yu, Recyclable nanoscale zero valent iron doped g-C<sub>3</sub>N<sub>4</sub>/MoS<sub>2</sub> for efficient photocatalysis of RhB and Cr (VI) driven by visible light, *ACS Sustainable Chem. Eng.*, 2016, **7**, 4055–4063.
- 69 X. Bai, Y. Y. Dua, X. Y. Hu, Y. D. He, C. L. He, E. Z. Liu and J. Fan, Synergy removal of Cr (VI) and organic pollutants over RP-MoS<sub>2</sub>/rGO photocatalyst, *Appl. Catal., B*, 2018, **239**, 204–213.
- 70 F. Martini, S. Borsacchi, G. Barcaro and M. Caporali, Phosphorene and Black Phosphorus: The <sup>31</sup>P NMR View, *J. Phys. Chem. Lett.*, 2019, (10), 5122–5127.
- 71 H. L. Yang, Y. Z. Liang, C. Wang, X. Song and Y. Q. Ge, Improved photocatalytic activity and stability of black phosphorus/multi-walled carbon nanotube hybrid for RhB degradation, *Nano.Tech.*, 2022, **33**, 185601.
- 72 M. Shalom, S. Inal, C. Fettkenhauer, D. Neher and M. Antonietti, Improving Carbon Nitride Photocatalysis by Supramolecular Preorganization of Monomers, *J. Am. Chem. Soc.*, 2013, **135**(19), 7118–7121.
- 73 Q. Hao, X. X. Niu, C. S. Nie, S. M. Hao, W. Zou, J. M. Ge and D. M. Chen, A highly efficient g-C<sub>3</sub>N<sub>4</sub>/SiO<sub>2</sub> heterojunction: the role of SiO<sub>2</sub> in the enhancement of visible light photocatalytic activity, *Phys. Chem. Chem. Phys.*, 2016, **18**, 31410–31418.
- 74 A. Hatamie, F. Marahel and A. Sharifat, Green synthesis of graphitic carbon nitride nanosheet (g-C<sub>3</sub>N<sub>4</sub>) and using it as a label-free fluorosensor for detection of metronidazole via quenching of the fluorescence, *Talanta*, 2018, **176**, 518–525.
- 75 E. Z. Liu, Y. N. Du, X. Bai, J. Fan and X. Y. Hu, Synergistic improvement of Cr (VI) reduction and RhB degradation using RP/g-C<sub>3</sub>N<sub>4</sub> photocatalyst under visible light irradiation, *Arabian J. Chem.*, 2020, **13**, 3836–3848.
- 76 S. Zhang, Y. G. Zhou, Y. Qi, J. Y. Shi, X. Y. Zhao and X. H. Zhang, TiO<sub>2</sub>-Photoanode-Assisted Direct-Solar-Energy Harvesting and Storage in a Solar-Powered Redox Cell Using Halides as Active Materials, *ACS Appl. Mater. Interfaces*, 2018, **27**, 23048–23054.
- 77 Y. Zhang, W. Q. Cui, W. J. An, L. Liu, Y. H. Liang and Y. F. Zhu, Combination of photoelectrocatalysis and adsorption for removal of bisphenol over TiO<sub>2</sub>-graphene hydrogel with 3D network structure, *Appl. Catal., B*, 2018, **221**, 36–46.

